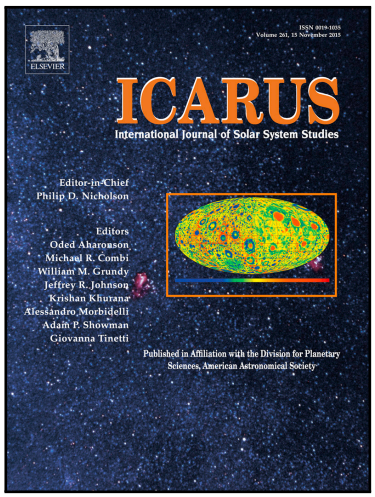

Cassini ISS Observation of Saturn's North Polar Vortex and Comparison to the South Polar Vortex

Kunio M. Sayanagi, John J. Blalock, Ulyana A. Dyudina, Shawn P. Ewald, Andrew P. Ingersoll

PII: S0019-1035(16)30817-X
DOI: 10.1016/j.icarus.2016.12.011
Reference: YICAR 12299

To appear in: *Icarus*

Received date: 16 February 2016
Revised date: 1 December 2016
Accepted date: 5 December 2016

Please cite this article as: Kunio M. Sayanagi, John J. Blalock, Ulyana A. Dyudina, Shawn P. Ewald, Andrew P. Ingersoll, Cassini ISS Observation of Saturn's North Polar Vortex and Comparison to the South Polar Vortex, *Icarus* (2016), doi: 10.1016/j.icarus.2016.12.011

Highlights

- We analyzed Saturns North Pole and South Pole as seen by Cassini Orbiter
- Our multispectral analysis reveal the cloud morphology of both of Saturns polar vortices
- Our analysis reveals detailed structure of the North Polar wind field.
- We reveal the presence a bright cloud feature that appears in short wavelengths over the south pole in 2007.
- We predict the formation of a bright feature over the north pole before the next equinox.

Cassini ISS Observation of Saturn's North Polar Vortex and Comparison to the South Polar Vortex

December 13, 2016

Kunio M. Sayanagi[1], John J. Blalock[1] Ulyana A. Dyudina[2], Shawn P. Ewald[2], Andrew P. Ingersoll,[2]

[1] *Department of Atmospheric and Planetary Sciences, Hampton University, Hampton, VA, 23668, USA*

[2] *Division of Geological and Planetary Sciences, California Institute of Technology, Pasadena, CA, 91125, USA*

Number of pages: 29

Number of tables: 2

Number of figures: 12

Proposed Running Head:

Cassini ISS Observation of Saturn's Polar Vortices

Please send Editorial Correspondence to:

Kunio M. Sayanagi

Department of Atmospheric and Planetary Sciences

Hampton University, Hampton, Virginia, 23668

Email: kunio.sayanagi@hamptonu.edu

ABSTRACT:

We present analyses of Saturn's north pole using high-resolution images captured in late 2012 by the Cassini spacecraft's Imaging Science Subsystem (ISS) camera. The images reveal the presence of an intense cyclonic vortex centered at the north pole. In the red and green visible continuum wavelengths, the north polar region exhibits a cyclonically spiraling cloud morphology extending from the pole to 85°N planetocentric latitude, with a 4700 km radius. Images captured in the methane bands, which sense upper tropospheric haze, show an approximately circular hole in the haze extending up to 1.5° latitude away from the pole. The spiraling morphology and the "eye"-like hole at the center are reminiscent of a terrestrial tropical cyclone. In the System III reference frame (rotation period of 10h39m22.4s, Seidelmann et al. 2007; Archinal et al. 2011), the eastward wind speed increases to about 140 m s^{-1} at 89°N planetocentric latitude. The vorticity is $(6.5\pm1.5)\times10^{-4}$ s^{-1} at the pole, and decreases to $(1.3\pm1.2)\times10^{-4}$ s^{-1} at 89°N. In addition, we present an analysis of Saturn's south polar vortex using images captured in January 2007 to compare its cloud morphology to the north pole. The set of images captured in 2007 includes filters that have not been analyzed before. Images captured in the violet filter (400 nm) also reveal a bright polar cloud. The south polar morphology in 2007 was more smooth and lacked the small clouds apparent around the north pole in 2012. Saturn underwent equinox in August 2009. The 2007 observation captured the pre-equinox south pole, and the 2012 observation captured the post-equinox north pole. Thus, the observed differences between the poles are likely due to seasonal effects. If these differences indeed are caused by seasonal effects, continuing observations of the summer north pole by the Cassini mission should show a formation of a polar cloud that appears bright in short-wavelength filters.

1 Introduction

On November 27, 2012, Cassini orbiter's Imaging Science Subsystem (ISS) camera returned high-resolution images of the north pole of Saturn illuminated by sunlight for the first time since the equinox in 1994. Before 1994, the northern high-latitudes were imaged by Voyager 1 & 2 in 1980 – 1981 (Godfrey, 1988), by the Hubble Space Telescope in 1990 (Caldwell et al., 1993), and by ground-based telescopes (Sanchez-Lavega et al., 1993, 1997). However, these images captured before the 1994 equinox did not resolve the north pole due to low image resolution and observation geometry that had severe foreshortening of the north pole.

When Cassini spacecraft entered orbit around Saturn in 2004, the northern high-latitudes were in winter polar night, and ISS, which senses scattered sunlight in visible and near-infrared wavelengths, was not able to image the pole. Prior to the present report, the Cassini Composite Infrared Spectrometer (CIRS) (Fletcher et al., 2008) observed thermal emissions from the polar region, and predicted cyclonic vorticity at the north pole. Observation by the Cassini Visible and Infrared Mapping Spectrometer (VIMS), whose 5-μm images reveal the motion of clouds silhouetted against the background thermal emissions, confirmed the strong cyclonic motion at the pole (Baines et al., 2009).

Sunlight started shining on the north pole of Saturn after the equinox in August 2009; however, Cassini had a poor view of the north pole until late 2012 because the orbiter stayed in an equatorial orbit. Using the 2012 data, we report the cloud morphology and wind field of Saturn's North Polar Vortex (NPV). Antuñano et al. (2015) previously measured the wind structure around both of the poles; our current wind measurements focus on a smaller region immediately around the north pole with a higher spatial resolution, and we also analyze the morphology in multiple wavelengths using different ISS filters. These images also captured the surrounding hexagonal jet pattern originally discovered by Godfrey (1988); our analysis of the hexagon will be reported separately.

The rest of our report is organized as follows. Section 2 describes the ISS image sets and the processing applied to them in our study. Section 3 presents our measurements of the

NPV. Section 4 compares the NPV to the South Polar Vortex observed earlier in the Cassini mission. Section 5 summarizes our results.

2 ISS Image Sets

We analyze both the north and south poles of Saturn in this report. To study the north pole, we analyze the Narrow-Angle Camera (NAC) images captured on November 27, 2012 and Wide-Angle Camera (WAC) images captured on December 10, 2012. For the south polar analysis, we examine WAC images captured between January 30 – 31, 2007, and NAC images captured on July 14, 2008. The imaging observation geometries of those image sequences are presented in Table 1. Previously, NAC images of the south pole captured in July – August 2004 were presented by Sánchez-Lavega et al. (2006) and those captured on October 11, 2006 were presented by Dyudina et al. (2008, 2009) and Antuñano et al. (2015). Antuñano et al. (2015) also analyzed CB2 and CB3 images captured in June – December 2013 of the north polar region. Our current report presents images captured using filters not included in these previous studies and/or in higher spatial resolution.

We follow the standard image calibration and processing procedure previously used by others to process ISS images of Saturn, e.g., Porco et al. (2005), Vasavada et al. (2006), Del Genio et al. (2007), and Sayanagi et al. (2013, 2014). We use the camera geometric model and the photometric calibration software CISSCAL version 3.4 described by Porco et al. (2004) and West et al. (2010) and released on April 9, 2006. The photometric flattening and mosaicing procedures are the same as in Sayanagi et al. (2013, 2014). Image navigation and map projection procedures used the equatorial and polar radii of 60,268 km and 54,364 km, respectively (Lindal et al., 1985). We use the System III longitude (rotation rate of $\Omega = 1.638\times10^{-4}$ s^{-1}, and rotation period of 10h39m22.4s; Seidelmann et al. 2007; Archinal et al. 2011). We use the planetocentric latitude throughout our report. We map the photometrically flattened images in polar orthographic projection such that our polar maps, centered on the pole, are re-sampled to 0.07° and 0.0028° of latitude per pixel for the WAC and NAC

images, respectively.

3 Analysis

3.1 Cloud Morphology

Figures 1 and 2 show the morphological context poleward of 83°N that surrounds the polar vortex captured in the WAC images. Figure 1 depicts the morphology captured in individual filters, and Fig. 2 presents color composites that combine views of multiple filters. Images captured in CB2 filter (757 nm continuum, Fig. 1a) show a spiraling cloud morphology poleward of 85°N. The sense of the spiral is cyclonic, i.e., the spiral arms turn counter-clockwise as they move away from the center. The NPV's appearances in RED (648 nm broadband, Fig. 1e) and GRN (567 nm broadband, Fig. 1f) filters are similar to that in CB2. In BL1 (460 nm broadband, Fig. 1g), and VIO (420 nm broadband, Fig. 1h), the spiraling morphology is barely discernible, and latitudes poleward of about 89.5°N are dark, appearing as a circular hole. In MT2 (728 nm moderate methane absorption band, Fig. 1c), the contrast is dominated by the dark circular hole centered on the pole and extending down to 88.5°N. The outline of the circular hole is sharp as will be further illustrated using the NAC images. In the MT2 view, the dark hole is surrounded by a gradual darkening toward the edge of the hole — the darkening becomes discernible poleward of 86.5°N. The same hole can be found in the MT3 view (889 nm strong methane absorption band, Fig. 1d); however, the contrast is much weaker than in MT2. We interpret the dark appearance of the pole in MT2, MT3, BL1 and VIO as a lack of reflecting aerosols rather than a presence of dark aerosols because no such darkening can be seen in CB2 and CB3. We also note that the size of this hole appears smaller in BL1 and VIO than in MT2 and MT3; since the methane absorption band filters MT2 and MT3 sense higher altitudes than the broad band visible filters BL1 and VIO, we interpret that the hole is larger in the upper altitudes sensed by the methane filters. The uniform scattering of shorter wavelengths BL1 and VIO in the region

outside the hole is also indicative of the presence of a layer of single-scattering particles smaller than ∼400 nm. Quantitative determination of the cloud and haze layer altitudes would require extensive radiative transfer modeling, which is beyond the scope of our study; García-Melendo et al. (2009, 2011) estimated that the CB2 filter senses altitudes between 350 mbar and 700 mbar, and MT2 and MT3 are sensitive to a range between 250 mbar and 60 mbar.

In Figs. 1d (MT3) and 1h (VIO), 29 and 30 images captured over 11h14m, respectively, were high-pass filtered and averaged to improve the image quality. In Figure 1d, the darkening at the corners is an artifact introduced by the spatial filtering, however, the circular feature centered on the pole is real. Note that the RED, GRN, BL1, VIO, MT2 and MT3 images have lower spatial resolution than the CB2 image because they were captured in 4×4 summation mode, which reduces the images to a 256×256 pixel resolution. The CB2 images were captured in the full 1024×1024 resolution.

Figure 2 shows color composite maps that combine views of multiple filters presented in Fig. 1. Figure 2a's red, green, and blue channels are assigned to CB2, MT2 and MT3 filters, respectively; a similar mosaic that overlaid CB2, MT2, BL1 and VIO was previously released as a press release PIA17652. In Fig. 2a, the region immediately around the pole appears red. We interpret this as a hole in the high-altitude haze layer to which the MT2 and MT3 images are sensitive, while the CB2 channel shows the top of the underlying cloud deck which does not have a hole at the pole. Because methane is well-mixed, features that appear bright in the MT2 and MT3 absorption bands must reside at high altitudes (Tomasko et al., 1984). Consequently, in this color scheme, the altitude of depicted features generally increases in order of red-green-blue — white indicates that light is scattered in all three wavelengths bands by aerosols at high altitudes; Sayanagi et al. (2013) used the same color scheme to show the great storm of 2010-2011 in their Figs. 4, 5, 11 and 16. Fig. 2b presents a real-color view of the pole, in which the RGB channels are assigned to RED, GRN, and BL1 images; this color scheme is the same as that of Sayanagi et al. (2013)'s Fig. 13.

High-resolution morphology of the center of the polar vortex is presented in Figs. 3, 4

and 5. Figure 3 presents the NAC view of the north pole; the figure shows a region within 1.5° of latitude around the pole. These images are processed such that the region poleward of 89° is from a single image, and the rest is a mosaic of multiple images to expand the view. The morphology in CB2, RED and GRN are very similar as exhibited in Fig. 2 panels a-c. In MT2, the circular hole in the upper tropospheric haze is apparent; this feature can also be seen in the WAC image (Fig. 1c). Inside of the hole, only the brightest of the features that are visible in Figs. 3a-c are apparent. The CB2 and MT2 images were captured in the full-resolution mode, while the RED, and GRN images were in the 2×2 summation mode.

Figure 4 shows the same region as in Fig. 3 in BL2 (Fig. 4a, 440 nm medium-band), UV3 (Fig. 4b, 343 nm broad-band) and MT3 (Fig. 4c) filters. These images are processed such that, for each of the filters, 7 images captured over 5 hours are averaged to improve the image contrast. In addition, for the UV3 images, high-pass spatial filter was applied to individual images prior to the averaging to remove contrast variation spanning more than 1300 km (approximately 1.4° in latitude) and compensate for the imperfections in the photometric flattening. Because the clouds in the polar vortex region move fast, in Fig. 4, the averaging operation smeared individual small clouds that are apparent in Fig. 3. We justify the averaging because those small features are difficult to distinguish from noise in the individual source images, and averaging multiple images helps in illustrating features symmetric around the pole. The BL2 view in Fig. 4a exhibits the same hole in the cloud previously presented in WAC views (BL1 and VIO, Figs. 1g and 1h). Unlike the hole's appearance in MT2, the hole's morphology in BL2 has a gradual contrast change, and lacks a clear outline. In UV3 (Fig. 4b), two concentric circular structures surround the hole. Figure 4c shows the view in MT3; the circular hole with a well-defined outline that roughly follows the 88.5°N latitude is the same feature as that seen in MT2 (Fig. 3d); however, no cloud feature is visible inside of the dark region. We did not find a high-latitude vortex that appears only in ultraviolet like that found on Jupiter by Porco et al. (2003).

Figure 5 shows the color overlay of the images that have been presented in Figs. 3 and 4. In Fig. 5a, the red, green and blue channels are assigned to CB2, MT2 and MT3,

respectively — this color scheme is the same as in Fig. 2a. A version without map-projection was previously released in a NASA press release PIA14944. In Fig. 5b, the red, green and blue channels are assigned to RED, GRN and BL2, respectively; this color scheme is the same as in Fig. 2b.

3.2 Cloud Tracking Wind Measurement

In this section, we present results of cloud-tracking wind measurement. To perform correlation imaging velocimetry (CIV) measurements, we use TRACKER3, a CIV tool developed at JPL and previously applied to analyze wind fields on Jupiter (Salyk et al., 2006) and Saturn (Sayanagi et al., 2013, 2014). We tracked cloud features in 14 of the NAC images captured over a period of 5 hour 19 min on November 27, 2012. During the imaging sequence, CB2 and RED images were captured alternately with a CB2-to-RED interval of about 20 minutes and RED-to-CB2 interval of about 29 minutes; we made CIV cloud-tracking measurements between these consecutive CB2 and RED images. In a CIV measurement, it is usually not ideal to use images captured using different filters that may sense features at different altitudes; however, in the current polar image sets, the appearance of cloud features is visually indistinguishable between CB2 and RED images (e.g., Fig 3a and 3b), and we found that the clouds in the region moved too fast around the pole to take measurements with ∼50-minute imaging intervals between images using a single filter. For these reasons, we found that it was more advantageous to track clouds between CB2 and RED images with 20 or 29 minute intervals. The images were mapped in polar orthographic projection as described in Section 2. Orthographic projection shortens the apparent distance by approximately 0.02 percent at 88.5°N, which does not pose an issue. Nevertheless, we circumvent the image distortion by measuring the latitude-longitude coordinates of the tracked clouds, and calculate their motion along Saturn's oblate spherical surface. Because the CB2 and RED images have different ranges of I/F values, the image contrast are normalized prior to performing our CIV measurements. To normalize the images' contrasts, they were first processed through

high-pass spatial filter to remove spacial structures larger than 250 km, and the contrasts were adjusted such that pixel brightness of all images had the same mean and standard deviation.

The images used for our CIV measurements are navigated using the spacecraft attitude data and planetary ephemeris provided by the Jet Propulsion Laboratory (JPL)'s Navigation and Ancillary Information Facility. Our past experience in navigating ISS WAC images (Sayanagi et al., 2013, 2014) informs us that the pointing information recorded by the spacecraft often have an error of one WAC pixel, or, 60 μradian. The pointing error could be corrected when the planetary limb is visible in the field of view of the camera; however, no limb was visible in the current set of polar images. Thus, as an alternative, we adjusted the maps so that the net large-scale translational motion between the mapped images is zero, which assumes that, on average, the zonal wind is symmetrical around the pole. Corrections up to an equivalent of 140 μradian of camera pointing were necessary to eliminate the net translational motion between the mapped images. It is possible that a real drifting motion of the polar vortex around the north pole is responsible for at least some of the net translational motion — such a "wobbling" motion of the polar vortex has been seen in models (e.g., O'Neill et al. 2015); however, here, the amplitude of the net translational motion seen in our data is comparable to the pointing uncertainties, and whether the north polar vortex of Saturn exhibits such a wobble remains inconclusive.

After the images were corrected for the net translational motion, they were then re-mapped into a reference frame in which Saturn rotated at 3.138×10^{-4} s^{-1}, i.e., 1.5×10^{-4} s^{-1} faster than the System III reference frame as defined by Seidelmann et al. (2007) and Archinal et al. (2011). The reference frame transformation was needed in order to reliably make the CIV measurements due to the fast eastward cloud motion in the region. In the transformed reference frame, the cloud motion due to the vortex's wind appears "frozen" near 88.95°N latitude. We did not change the resolution and the domain in the re-mapping process, and resulting maps retain the 1024×1024-pixel polar orthographic projection as described in Section 2.

The CIV measurements presented in this report used the following parameters. The correlation box size was set to 30×30 pixels (78×78 km; 78 km is approximately 0.084° in latitude near the pole), which roughly corresponds to the size of typical clouds resolved in the NAC images. A tracking measurement was made on a cartesian grid with a grid separation of 5 pixels (∼13 km), i.e., there is a significant overlap in the correlation box between the grids to ensure continuity in the returned wind field. The correlation algorithm searched for a matching morphology in distance up to 80 pixels away in the polar orthographic maps (about 210 km). For an image pair with 20-minute temporal separation, this correlation search range combined with the reference frame change to 3.138×10^{-4} s^{-1} makes our measurements sensitive to wind speeds up to 175 m s^{-1} at the pole and zonal wind speeds between 35 m s^{-1} and 315 m s^{-1} at 89°N.

The zonal mean wind profiles returned by our cloud-tracking wind measurements are shown in Fig. 6. Figure 6d shows the distribution of the wind vector as a function of latitude; our analysis returned a total of 274,822 wind vectors; we binned the wind vectors in latitude with a bin width of 0.01°. The zonal mean and standard deviation of the eastward wind component u are presented in Figs. 6a. Here, the zonal standard deviation of u and v are the longitudinal variations in the measured value of u and v; they do not represent measurement uncertainties. The zonal wind speed steadily increases from the north pole to the end of the measurement at 88.5°N latitude. The zonal mean of the meridional wind component v, shown in Fig. 6b, is essentially zero throughout the domain of measurement. The mapping process we used forces the domain-mean meridional wind to become zero; however, our measurements are sensitive to residual fluctuations around zero. Thus, our measurements did not detect zonally organized convergence or divergence centered on the pole. The zonal standard deviations of both u and v stay between 3.7 m s^{-1} (at 89.52°N) and 16 m s^{-1} (at 88.5°N) throughout the latitudes covered in the measurement.

The values of standard deviations include contributions from both real spatial variation in the wind and the uncertainty in the wind measurements. Although our measurements do not provide a direct way to distinguish the true spatial variations and the measurement

uncertainty, the zonal standard deviations of u and v can be used to separate contributions from anisotropic component of the spatial variation from the isotropic variation. Figure 6c presents the zonal standard deviations of u and v; when the values of standard deviations are different, the wind vector variation is spatially anisotropic. The maximum anisotropy occurs at 89.22°N latitude, where the standard deviation of u is 5.7 m s^{-1} greater than that of v; if we assume that our measurement uncertainty is isotropic, we can attribute this anisotropy in the wind vector variations to real spatial structures. The standard deviations of u and v are essentially the same at 5-7 m s^{-1} between 89.4°N and 89.8°N latitudes, thus the wind vector variations are spatially isotropic at these latitudes. However, the uncertainties of CIV cloud tracking methods are highly dependent on the cloud morphology. At 89.22°N, Fig. 3a shows that the clouds appear as streaks oriented in east-west directions, which increases the uncertainty of u; consequently, it is not surprising that the standard deviation of u is greater than that of v. In the worst case, the measurement uncertainty is responsible for all of the standard deviation. We expect that, even in the absolute worst case, the correlation feature match can have a tracking uncertainty of quarter of the correlation box size, which is about 15 km in our current measurement. This would result in the wind speed uncertainty of 16 m s^{-1}; Fig. 6c shows that the zonal standard deviations of u and v are substantially smaller than 16 m s^{-1} in almost all latitudes. As a reference, for an image pair with 20 minute temporal separation, the uncertainty of 10 m s^{-1} and 5 m s^{-1} would represent a tracking uncertainty of about 12 km and 6 km, respectively. Those uncertainties correspond to about 15 percent and 7.5 percent of the size of the correlation box, or 4.3 pixels and 2.2 pixels in the polar-projected maps, respectively.

3.3 Relative Vorticity and Divergence

In this subsection, we present the relative vorticity and divergence of the wind field in the north polar vortex. We calculate the vorticity and divergence using the results of the cloud-tracking wind measurements presented in the previous subsection. We first fill the gaps in the

wind field using bi-linear interpolation. Figures 7a and 7b present the zonal and meridional wind components of the cloud-tracking measurements — the cloud tracking result shown in Fig. 7 is from the cloud tracking performed between cloud maps presented in Figs. 3a and 3b. In the figures, the black pixels represent areas where no trackable pattern was detected. Figures 7c and 7d show the same wind fields with the gaps interpolated. The vorticity and divergence were calculated using the interpolated wind field.

After the gaps in the wind field are filled through interpolation, we calculate the relative vorticity and divergence. Our wind vectors are calculated on a cartesian grid (i, j) superimposed on the polar orthographic map projection. The cartesian grid indices i and j increase in the directions of 0° and 90° eastward longitude, respectively. We denote the cartesian wind components as $U_{i,j}$ and $V_{i,j}$. $U_{i,j}$ and $V_{i,j}$ blow in the direction of 0° and 90° eastward longitude, respectively. The cartesian wind components $U_{i,j}$ and $V_{i,j}$ are related to the eastward and northward wind components $u_{i,j}$ and $v_{i,j}$ by

$$\begin{aligned} U_{i,j} &= -u_{i,j}\sin(\lambda_{i,j}) - v_{i,j}\cos(\lambda_{i,j}) \\ V_{i,j} &= u_{i,j}\cos(\lambda_{i,j}) - v_{i,j}\sin(\lambda_{i,j}), \end{aligned} \tag{1}$$

where $\lambda_{i,j}$ is the eastward longitude. On grid $(i,\ j)$, the relative vorticity then becomes

$$\zeta_{i,j} = \frac{V_{i+1,j} - V_{i-1,j}}{\Delta X_{i,j}} - \frac{U_{i,j+1} - U_{i,j-1}}{\Delta Y_{i,j}}. \tag{2}$$

Similarly, the divergence is

$$\delta_{i,j} = \frac{U_{i,j+1} - U_{i,j-1}}{\Delta X_{i,j}} + \frac{V_{i,j+1} - V_{i,j-1}}{\Delta Y_{i,j}}. \tag{3}$$

We take account of Saturn's oblateness in calculating the distances $\Delta X_{i,j}$ and $\Delta Y_{i,j}$ using the following oblate spherical mapping factors

$$r_{i,j} = \frac{R_\mathrm{e}}{1 + (R_\mathrm{p}/R_\mathrm{e})^2 \tan^2\varphi_{i,j}} \tag{4}$$

and

$$R_{i,j} = \frac{r_{i,j}/\cos\varphi_{i,j}}{\sin^2\varphi_{i,j} + (R_\mathrm{e}/R_\mathrm{p})^2\cos^2\varphi_{i,j}} \tag{5}$$

where R_e and R_p are equatorial and polar radii, respectively. $r_{i,j}$ is the distance of point (i, j) from the planet's rotation axis, and $R_{i,j}$ is the radius of curvature of the local meridian. $\varphi_{i,j}$ is the planetographic latitude, which is related to the planetocentric latitude $\theta_{i,j}$ by

$$\varphi_{i,j} = \arctan\left((R_\mathrm{e}/R_\mathrm{p})^2 \tan\theta_{i,j}\right). \tag{6}$$

Using these mapping factors, $\Delta X_{i,j}$ and $\Delta Y_{i,j}$ become

$$\begin{aligned} \Delta X_{i,j} &= \left(r_{i,j}^2(\lambda_{i+1,j} - \lambda_{i-1,j})^2 + R_{i,j}^2(\varphi_{i+1,j} - \varphi_{i-1,j})^2\right)^{1/2} \\ \Delta Y_{i,j} &= \left(r_{i,j}^2(\lambda_{i,j+1} - \lambda_{i,j-1})^2 + R_{i,j}^2(\varphi_{i,j+1} - \varphi_{i,j-1})^2\right)^{1/2}. \end{aligned} \tag{7}$$

The values of ΔX and ΔY vary between about 32.648 km and 32.651 km in the domain of this calculation.

Figure 8 presents the result of the relative vorticity and divergence calculations. Figure 8a shows that the relative vorticity is entirely cyclonic in the polar region, and peaks around the north pole. The cyclonic shear is also apparent in the zonal mean wind profile presented in Fig. 6a. The divergence in the region is significantly smaller than the relative vorticity. The map of divergence shows a fluctuation around zero. Like the wind vectors, the variations in the relative vorticity and divergence represent the sum of real spatial variations and measurement uncertainties. Here, we suspect that the variation in the divergence is dominated by the uncertainties in the wind measurements but we present its map nevertheless to demonstrate that such fluctuations are generally small in spatial scales, and large values are confined to limited areas.

The zonal means of the relative vorticity and divergence are presented in Fig. 9. Here, the zonal mean and standard deviation are calculated by latitudinally binning the two-dimensional relative vorticity and divergence fields computed from cloud tracking results of all 13 image pairs, not only for the data shown in Figure 8. The two-dimensional vorticity and divergence measurements are binned in latitude with a bin size of 0.01°; we emphasize that the zonal mean of the relative vorticity and divergence, shown in Fig. 9, were *not* computed from the zonal mean of u and v shown in Fig. 6. The magnitudes of the standard deviation as functions of latitude are approximately the same for the relative vorticity and divergence

(between 0.5×10^{-4} s^{-1} and 1.5×10^{-4} s^{-1}), which suggest that their zonal standard deviation is more representative of measurement uncertainties rather than real spatial variation, or the divergence and relative vorticity are correlated. The cyclonic relative vorticity peaks at the pole at $\sim6\times10^{-4}$ s^{-1}, which is twice as much as Saturn's planetary vorticity, 3.3×10^{-4} s^{-1}. The relative vorticity of the north pole measured using VIMS images (Baines et al., 2009) peaked at $\sim5\times10^{-4}$ s^{-1}; we believe that the difference is due to the coarser resolution of the VIMS instrument. The relative vorticity analysis by Antuñano et al. (2015) gives a value of $(2.5 \pm 0.1) \times 10^{-4}$ s^{-1} at 89.8°N, which is less than half of our measurement; this difference is likely due to a combination of using lower-resolution wind measurement and employing spatial averaging — in Antuñano et al. (2015)'s measurements, wind vectors were placed on a cartesian grid with $\Delta x \sim \Delta y \sim 285$ km and then averaged over 1,140 km. The relative vorticity of the south-polar vortex measured using ISS images (Dyudina et al., 2009; Antuñano et al., 2015) peaked at approximately -3×10^{-4} s^{-1}. In comparison, owing to their small radius and relatively fast wind, the center of terrestrial hurricanes can reach relative vorticity of $\sim7\times10^{-3}$ s^{-1} within 20 km of the center of the eye (e.g., Judt and Chen 2010).

We note that different conventions have been employed in the sign of the vorticity in the polar regions of Saturn. Dyudina et al. (2009) used a definition that made the sign of the relative vorticity positive for the cyclonic south polar vortex (defined by the first equation in their Section 4). Baines et al. (2009) used the same definition as Dyudina et al. (2009) to define vorticity, resulting a negative sign of vorticity for the cyclonic north polar vortex. Antuñano et al. (2015) employs a conventional definition of relative vorticity (their Eq. 4); however, their calculation contains a sign error, resulting in a negative sign of relative vorticity for the cyclonic north polar vortex. In this report, we use a conventional definition of the relative vorticity in which a cyclonic vortex has a positive relative vorticity in the northern hemisphere.

4 Comparison to Saturn's South Pole

In this section, we compare the cloud morphology of the north-polar vortex to that of the south-polar vortex. The morphology and dynamics of Saturn's south pole has been documented previously by Sánchez-Lavega et al. (2006), Dyudina et al. (2008, 2009) and Antuñano et al. (2015). These previous papers presented the morphology of the south pole using CB2 and CB3 images, which showed, like the north pole, the clouds around the south pole exhibit cyclonically spiraling (i.e., a spiral arm turns counterclockwise as it extends away from the pole) morphology centered on the pole and extending down to around 83°S.

Here, we extend the morphological analysis to the images captured using MT2, MT3, RED, GRN, BL1 and VIO filters in addition to CB2 and CB3. On January 30-31, 2007, 9 images were captured in each of the filters over a duration of 3 hour 20 minute; we averaged the 9 map-projected images captured in each of the filters to improve the contrast, and show the results for each of the filters in Figure 10.

Figure 10 presents polar-projected maps of the southern high-latitude region. The double-wall structure surrounding the "eye" of the south polar vortex, originally reported by Dyudina et al. (2008), is apparent when viewed in CB2 (Fig. 10a), CB3 (10b), RED (10e), GRN (10f) and BL1 (10g). The two walls are located at ∼88°S and ∼89°S. In those filters, the interior of the eye appears dark. Outside of the eye, concentric albedo structure that appears substantially brighter than the eye interior dominates the morphology, in which a few diffuse discrete features can also be seen. The interior of the eye also appears dark in MT2 (Fig. 10c) and MT3 (10d). While the interior of the eye of the south-polar vortex appears darker than the surrounding in all above filters, the contrast is reversed in VIO (Fig. 10h), in which a bright cloud covers the south-polar vortex eye region poleward of 87°S, which we call the polar cap. The bright polar cap is apparent only in the VIO filter presumably because the aerosol layer that forms the cap is in the stratosphere, where it scatters light more in the shorter wavelengths sensed by the VIO filter.

The presence of the bright cap visible in VIO is consistent with the warm summer south

polar region observed by Cassini CIRS (Fletcher et al., 2008, 2015). Fletcher et al. (2008, 2015) interpreted the warming of the south pole to be a result of solar absorption by stratospheric aerosols formed through photodissociation of methane molecules and trapped in the south polar vortex. Our observation of the bright polar cap over the south pole (Fig. 10h) was taken in 2007 shortly before the equinox in 2009 (late summer), while the north polar images without a cap were captured in 2012 (early spring). The photochemical production of haze particles in giant planet stratospheres is described by Atreya and Wong (2005), Wong et al. (2003) and West et al. (2009). Like Fletcher et al. (2008, 2015), we interpret the presence of a haze layer over the summer pole as an indication that it is a result of ultraviolet photodissociation of hydrocarbon molecules in the summer polar stratosphere. If Saturnian bright polar caps consist of aerosols formed through ultraviolet photodissociation of hydrocarbons, it also explains the absence of a similar cap over the north pole in 2012 because the north polar region had not received sufficient insolation to have formed a photochemical haze layer. This hypothesis may be tested by the Cassini extended mission by observing whether a cap similar to that seen over the south pole in 2007 will form over the north pole as the north pole approaches the next solstice in 2017.

As shown in Fig. 10c, in MT2, the brightness of the eye interior appears to decrease in three discrete steps; the clouds appear the brightest outside of the outer wall at 87°S latitude. The region between 87°S and 88°S (which roughly coincides the outer edge of the inner wall structure) constitutes the first step down in the albedo value. The region between 88°S and 89°S forms the second step. Poleward of 89°S is the third step, where the albedo is the darkest in the south-polar region seen in MT2; 89°S roughly corresponding to the inner edge of the the inner wall structure. The morphology in MT3 appears (Fig. 10d) generally similar to that in MT2, except that the boundaries between the albedo steps are not as sharp.

Figure 11a presents a false-color view in which red, green and blue channels are assigned to CB2, MT2, and MT3 maps like in Fig. 2a and Fig. 5a. Figure 11b assigns the RGB channels to RED, GRN and BL1 maps like in Fig. 2b and Fig. 5b, showing a contrast-enhanced real

color view of the south pole.

We also analyze the morphologies and the motions of clouds inside the south polar vortex's inner eye-wall, shown in Fig. 12. Three NAC images captured using the CB2 filter on July 14, 2008 revealed multiple discrete clouds that can be tracked over two hours. The first of the three images is shown in Figs. 12a (with feature labels) and 12e (without labels). Features A and F have well-defined oval shapes with sharply resolved outlines. Features B, C, D, E and H also have oval shapes, but have gradually fading boundaries. Features A, C, D and E have filamentary clouds that appear to reside at a higher altitude, which may or may not be dynamically linked to the underlying oval. Feature G is a filamentary structure without an underlying oval. Table 2 summarizes the features displayed in Fig. 12. Features inside the south-polar vortex's eye were also noted by lower-resolution images presented by Dyudina et al. (2009) (see their Figs. 3 and 4 in particular).

Figure 12 shows that these features, all located near 89.4°S latitude (except Feature H, which is placed nearly over the south pole and stationary), move at similar speeds with respect to the System III reference frame. To illustrate the motions of features A-H, Figs. 12b and 12c show the same region shown in 45 min and 112 min after the first frame shown in Fig. 12a, respectively. Fig. 12d overlays the first, second and third images in the System III frame in red, yellow, green colors, showing that all features generally rotate clockwise (i.e., eastward) in this reference frame. The second and third images shown again in Figs. 12f and 12g, which are drawn to "freeze" the motion of the clouds by mapping them in a reference frame rotating at 0.48° minute^{-1} (1.4×10^{-4} radian s^{-1}) in the counterclockwise direction with respect to System III. Fig. 12h show a color overlay similar to 12d in the transformed reference frame, which shows residual motions of the clouds with respect to the imposed rotation. This rotating motion corresponds to relative vorticity of -2.8×10^{-4} s^{-1} (which is cyclonic), and, at 89.4°S, the wind speed is ∼80 m s^{-1} with respect to System III. Our vorticity estimate for the south pole is similar to the value measured by Antuñano et al. (2015).

In addition, the internal vorticity of two of the features can be seen in Fig. 12. Feature

A exhibits a counterclockwise rotation when panels e-g are overlayed in panel h — the oval's orientation rotates counterclockwise in the rotation corrected reference frame shown in panels e-h, and the overlying filamentary clouds also show a counterclockwise circulation, hinting that Feature A is an anticyclone. On the other hand, Feature D's overlying spiral cloud shows a clockwise circulation, from which we infer that the feature is cyclonic. We were unable to perform automated cloud-tracking analysis on the south polar data because, unlike the north polar data we presented in Section 3.2, the south pole does not have sufficient number of trackable features for the cloud-tracking method to be effective.

5 Summary of Results

The north-polar observations by Cassini in November 2012 revealed the cloud morphology of the north-polar vortex illuminated by sunlight. We used the high-resolution images returned by the ISS camera to perform cloud-tracking wind measurements. We also compared the new observation of the north pole to the south pole observed in 2006 and 2007. Our results can be summarized as follows.

1. The dominant feature of the north-polar cloud morphology observed in images captured in the CB2, CB3, RED and GRN filters is a cyclonic spiral centered at the pole and extending to ∼85°N latitude with a radius of 4700 km. The spiralling morphology of the deep cloud sensed in the CB2, CB3, RED and GRN filters are consistent with the Cassini VIMS 5-micron observations documented by Baines et al. (2009).

2. The upper tropospheric haze layer detected in the MT2, MT3, BL1 and VIO filters shows a dark circular hole centered at the pole. In the MT2 and MT3 filters, the outline of the hole, located at 88.5°N latitude, is sharp. The hole seen in the BL1 and VIO shows a gradual poleward darkening starting around ∼88.5°. These filters are sensitive to the haze layer in the upper troposphere and lower stratosphere. We interpret the dark appearance of

the pole in these filters as a hole in the upper tropospheric haze layer rather than a region of dark aerosols because no such darkening toward the pole is seen in CB2 and CB3, which sense the top of tropospheric deep cloud deck.

3. The north polar region has an intense cyclonic vortex centered at the pole. The zonal mean eastward wind component increases from zero at the north pole to 150 m s^{-1} eastward at 89.0°, exhibiting a strong cyclonic wind shear. The wind speeds detected here are consistent with that measured by Baines et al. (2009) for the north pole. The wind structure at the north pole is similar to that at the south pole revealed by Baines et al. (2009) and Dyudina et al. (2009).

4. The relative vorticity peaks at $\sim 6 \times 10^{-4}$ s^{-1} at the north pole, which is a factor of two greater than the planetary vorticity. The value measured here is greater than the values previously measured by Antuñano et al. (2015) ($(2.5 \pm 0.1) \times 10^{-4}$ s^{-1}) using lower-resolution ISS images, and Baines et al. (2009) ($(5 \pm 0.5) \times 10^{-4}$ s^{-1}) using VIMS 5-micron images; we believe that these earlier measurements did not resolve the peak at the pole due to the lower resolutions of the images employed in their studies. In numerical simulations by O'Neill et al. (2015, 2016) for a Saturn-like case, the vortices gain relative vorticity of up to 1.5 times the planetary vorticity. The dynamical implication of the high polar relative vorticity value is unclear.

5. The magnitude of the zonal mean divergence of the wind field is smaller than 10^{-5} s^{-1}, beyond the detection limit of the current study.

6. The south polar vortex exhibits two concentric eye walls at ∼88°S and ∼89°S in CB2, CB3, RED, GRN and BL1 wavelengths.

7. In 2007, the south polar region at latitudes higher than ∼87°S was covered in a bright

polar cap visible in the VIO filter. We interpret the presence of the cap in the summer pole as a result of stratospheric photochemical haze production through mechanisms described by Atreya and Wong (2005), Wong et al. (2003) and West et al. (2009). If the haze particles indeed form over a summer pole, we expect a similar polar cap to form over the north pole as it approaches the next solstice in 2017.

8. Discrete clouds can be seen in the interior of the inner eye wall of the south polar vortex. From the motion of the clouds, the relative vorticity is estimated to be $-2.8{\times}10^{-4}$ s^{-1} (which is cyclonic). The relative vorticity structure of the south pole measured by Dyudina et al. (2009) and Antuñano et al. (2015) was 3×10^{-4} s^{-1}.

The Cassini discoveries of intense polar cyclones at both poles of Saturn are intriguing. Scott (2011), O'Neill et al. (2015, 2016) and Brueshaber and Sayanagi (2014) used numerical models to show that turbulence leads to poleward flux of cyclonic vorticity through beta-drifting cyclones, and results in an accumulation of cyclonic vorticity at the pole. In particular, O'Neill et al. (2015, 2016) demonstrated that the ratio of the planetary radius a and the Rossby deformation radius L_{D} is a key parameter that controls giant planet polar atmospheric dynamics. They showed that an intense polar vortex forms when the model used a strong turbulent forcing and a Saturn-like size ratio of $a/L_{\mathrm{D}} \sim 20$; under this regime, the relative vorticity of the polar vortex became greater than the planetary vorticity by a factor of ∼1.5. Under weak mechanical forcing and $a/L_{\mathrm{D}} \sim 20$, O'Neill et al. (2015) produced a transient polar cyclone, which the authors hypothesized as a Neptune-like regime. For a Jupiter-like planetary size ratio of $a/L_{\mathrm{D}} \sim 40$, the model produced turbulent flows with weak zonal organization like that of Jupiter's high latitudes regardless of the forcing strength.

Comparison of the Saturnian polar vortices with terrestrial cyclones illustrates some interesting commonalities and differences between them. First, terrestrial hurricanes require a warm sea surface to form (Anthes, 1982; Houze, 1993; Emanuel, 2003); such an energy

source is not available on the giant planets. Although the formation process differs, the intensification of terrestrial hurricanes follows a process similar to that tested by Scott (2011) and O'Neill et al. (2015, 2016). In addition to the latent heat flux from the surface, when a terrestrial tropical cyclone becomes intense enough, it creates a local peak in the potential vorticity field such that it generates a local *effective* β-effect. The process involving local effective-β is analogous to the planetary-β, which is the gradient of the planetary vorticity, and the results are similar; when cumulus convection generates eddies inside of a terrestrial tropical cyclone, it causes an inward flux of cyclonic vorticity, and intensifies the cyclone (Montgomery and Enagonio, 1998). Further modeling efforts under more realistic conditions (e.g., inclusion of the vertical dimension so that baroclinic effects are realistically represented) and observational studies to measure the eddy momentum flux in the polar region (such measurements have been performed for mid-latitudes by Del Genio et al. (2007) and Del Genio and Barbara (2012)) may shed further light on this process.

If the differences in the morphology between the south pole in 2007 and the north pole in 2012 were caused by seasonal effects, the north pole, now basking in continuous sunshine, should become similar that of the south pole in 2007. In particular, if the polar cap over the south pole in 2007, seen in the VIO filter (Fig. 10h), is produced through ultraviolet photodissociation of hydrocarbon molecules, we expect a similar bright cap to form over the north pole later in the season. The continuing observation by the Cassini mission should reveal whether seasonal effects will alter the polar cloud morphology.

Acknowledgements

Our work was supported by the Cassini-Huygens mission, a cooperative project of NASA, ESA, ASI, managed by JPL, a division of the California Institute of Technology, under a contract with NASA. KMS acknowledges support from NASA Outer Planets Research Grant NNX12AR38G, NASA Planetary Atmospheres Program Grant NNX14AK07G, NASA Cassini Data Analysis Program Grant NNX15AD33G, and NSF Astronomy and Astrophysics Grant 1212216. API acknowledges support from NSF grant AST-1411952 and by the Cassini

559 Project of NASA.

560 References

561 Anthes, R. A., 1982. Tropical Cyclones. Their Evolution, Structure and Effects. American
562 Meteorological Society.

563 Antuñano, A., Río-Gaztelurrutia, T., Sánchez-Lavega, A., Hueso, R., 2015. Dynamics of
564 Saturn's polar regions. Journal of Geophysical Research (Planets) 120, 155–176.

565 Archinal, B. A., A'Hearn, M. F., Bowell, E., Conrad, A., Consolmagno, G. J., Courtin, R.,
566 Fukushima, T., Hestroffer, D., Hilton, J. L., Krasinsky, G. A., Neumann, G., Oberst, J.,
567 Seidelmann, P. K., Stooke, P., Tholen, D. J., Thomas, P. C., Williams, I. P., 2011. Report
568 of the IAU Working Group on Cartographic Coordinates and Rotational Elements: 2009.
569 Celestial Mechanics and Dynamical Astronomy 109, 101–135.

570 Atreya, S. K., Wong, A.-S., 2005. Coupled Clouds and Chemistry of the Giant Planets — A
571 Case for Multiprobes. Space Science Reviews 116, 121–136.

572 Baines, K. H., Momary, T. W., Fletcher, L. N., Showman, A. P., Roos-Serote, M., Brown,
573 R. H., Buratti, B. J., Clark, R. N., Nicholson, P. D., 2009. Saturn's north polar cyclone and
574 hexagon at depth revealed by Cassini/VIMS. Planetary and Space Science 57, 1671–1681.

575 Brueshaber, S. R., Sayanagi, K. M., 2014. Numerical Simulations of Saturn's Polar Cyclones.
576 In: AAS/Division for Planetary Sciences Meeting Abstracts. Vol. 46 of AAS/Division for
577 Planetary Sciences Meeting Abstracts. p. 422.27.

578 Caldwell, J., Hua, X.-M., Turgeon, B., Westphal, J. A., Barnet, C. D., 1993. The drift of
579 Saturn's north polar SPOT observed by the Hubble Space Telescope. Science 260, 326–329.

580 Del Genio, A. D., Barbara, J. M., 2012. Constraints on Saturn's tropospheric general circu-
581 lation from Cassini ISS images. Icarus 219, 689–700.

582 Del Genio, A. D., Barbara, J. M., Ferrier, J., Ingersoll, A. P., West, R. A., Vasavada, A. R.,
583 Spitale, J., Porco, C. C., 2007. Saturn eddy momentum fluxes and convection: First
584 estimates from Cassini images. Icarus 189, 479–492.

585 Dyudina, U. A., Ingersoll, A. P., Ewald, S. P., Vasavada, A. R., West, R. A., Baines, K. H.,
586 Momary, T. W., Del Genio, A. D., Barbara, J. M., Porco, C. C., Achterberg, R. K., Flasar,
587 F. M., Simon-Miller, A. A., Fletcher, L. N., 2009. Saturn's south polar vortex compared
588 to other large vortices in the Solar System. Icarus 202, 240–248.

589 Dyudina, U. A., Ingersoll, A. P., Ewald, S. P., Vasavada, A. R., West, R. A., Del Genio,
590 A. D., Barbara, J. M., Porco, C. C., Achterberg, R. K., Flasar, F. M., Simon-Miller, A. A.,
591 Fletcher, L. N., 2008. Dynamics of Saturn's South Polar Vortex. Science 319, 1801–.

592 Emanuel, K., 2003. Tropical Cyclones. Annual Review of Earth and Planetary Sciences 31,
593 75–104.

594 Fletcher, L. N., Irwin, P. G. J., Orton, G. S., Teanby, N. A., Achterberg, R. K., Bjoraker,
595 G. L., Read, P. L., Simon-Miller, A. A., Howett, C., de Kok, R., Bowles, N., Calcutt,
596 S. B., Hesman, B., Flasar, F. M., 2008. Temperature and Composition of Saturn's Polar
597 Hot Spots and Hexagon. Science 319, 79–81.

598 Fletcher, L. N., Irwin, P. G. J., Sinclair, J. A., Orton, G. S., Giles, R. S., Hurley, J., Gorius,
599 N., Achterberg, R. K., Hesman, B. E., Bjoraker, G. L., 2015. Seasonal evolution of Saturn's
600 polar temperatures and composition. Icarus 250, 131–153.

601 García-Melendo, E., Pérez-Hoyos, S., Sánchez-Lavega, A., Hueso, R., 2011. Saturn's zonal
602 wind profile in 2004-2009 from Cassini ISS images and its long-term variability. Icarus
603 215, 62–74.

604 García-Melendo, E., Sánchez-Lavega, A., Rojas, J. F., Pérez-Hoyos, S., Hueso, R., 2009.
605 Vertical shears in Saturn's eastward jets at cloud level. Icarus 201, 818–820.

606 Godfrey, D. A., 1988. A hexagonal feature around Saturn's North Pole. Icarus 76, 335–356.

607 Houze, R. A., 1993. Cloud Dynamics. Academic Press, San Diego, CA.

608 Judt, F., Chen, S. S., 2010. Convectively Generated Potential Vorticity in Rainbands and
609 Formation of the Secondary Eyewall in Hurricane Rita of 2005. Journal of Atmospheric
610 Sciences 67, 3581–3599.

611 Lindal, G. F., Sweetnam, D. N., Eshleman, V. R., 1985. The atmosphere of Saturn - an
612 analysis of the Voyager radio occultation measurements. Astronomical Journal 90, 1136–
613 1146.

614 Montgomery, M. T., Enagonio, J., 1998. Tropical Cyclogenesis via Convectively Forced Vor-
615 tex Rossby Waves in a Three-Dimensional Quasigeostrophic Model. Journal of Atmo-
616 spheric Sciences 55, 3176–3207.

617 O'Neill, M. E., Emanuel, K. A., Flierl, G. R., 2015. Polar vortex formation in giant-planet
618 atmospheres due to moist convection. Nature Geoscience 8, 523–526.

619 O'Neill, M. E., Emanuel, K. A., Flierl, G. R., 2016. Weak Jets and Strong Cyclones: Shallow-
620 Water Modeling of Giant Planet Polar Caps. Journal of Atmospheric Sciences 73, 1841–
621 1855.

622 Porco, C. C., Baker, E., Barbara, J., Beurle, K., Brahic, A., Burns, J. A., Charnoz, S.,
623 Cooper, N., Dawson, D. D., Del Genio, A. D., Denk, T., Dones, L., Dyudina, U., Evans,
624 M. W., Giese, B., Grazier, K., Helfenstein, P., Ingersoll, A. P., Jacobson, R. A., Johnson,
625 T. V., McEwen, A., Murray, C. D., Neukum, G., Owen, W. M., Perry, J., Roatsch, T.,
626 Spitale, J., Squyres, S., Thomas, P., Tiscareno, M., Turtle, E., Vasavada, A. R., Veverka,
627 J., Wagner, R., West, R., 2005. Cassini Imaging Science: Initial Results on Saturn's
628 Atmosphere. Science 307, 1243–1247.

629 Porco, C. C., West, R. A., McEwen, A., Del Genio, A. D., Ingersoll, A. P., Thomas, P.,
630 Squyres, S., Dones, L., Murray, C. D., Johnson, T. V., Burns, J. A., Brahic, A., Neukum,

631 G., Veverka, J., Barbara, J. M., Denk, T., Evans, M., Ferrier, J. J., Geissler, P., Helfen-
632 stein, P., Roatsch, T., Throop, H., Tiscareno, M., Vasavada, A. R., 2003. Cassini Imaging
633 of Jupiter's Atmosphere, Satellites, and Rings. Science 299, 1541–1547.

634 Porco, C. C., West, R. A., Squyres, S., McEwen, A., Thomas, P., Murray, C. D., Del Genio,
635 A., Ingersoll, A. P., Johnson, T. V., Neukum, G., Veverka, J., Dones, L., Brahic, A.,
636 Burns, J. A., Haemmerle, V., Knowles, B., Dawson, D., Roatsch, T., Beurle, K., Owen,
637 W., 2004. Cassini Imaging Science: Instrument Characteristics And Anticipated Scientific
638 Investigations At Saturn. Space Science Reviews 115, 363–497.

639 Salyk, C., Ingersoll, A. P., Lorre, J., Vasavada, A., Del Genio, A. D., 2006. Interaction
640 between eddies and mean flow in Jupiter's atmosphere: Analysis of Cassini imaging data.
641 Icarus 185, 430–442.

642 Sánchez-Lavega, A., Hueso, R., Pérez-Hoyos, S., Rojas, J. F., 2006. A strong vortex in
643 Saturn's South Pole. Icarus 184, 524–531.

644 Sanchez-Lavega, A., Lecacheux, J., Colas, F., Laques, P., 1993. Ground-based observations
645 of Saturn's north polar SPOT and hexagon. Science 260, 329–332.

646 Sanchez-Lavega, A., Rojas, J. F., Acarreta, J. R., Lecacheux, J., Colas, F., Sada, P. V.,
647 1997. New Observations and Studies of Saturn's Long-Lived North Polar SPOT. Icarus
648 128, 322–334.

649 Sayanagi, K. M., Dyudina, U. A., Ewald, S. P., Fischer, G., Ingersoll, A. P., Kurth, W. S.,
650 Muro, G. D., Porco, C. C., West, R. A., 2013. Dynamics of Saturn's great storm of 2010-
651 2011 from Cassini ISS and RPWS. Icarus 223, 460–478.

652 Sayanagi, K. M., Dyudina, U. A., Ewald, S. P., Muro, G. D., Ingersoll, A. P., 2014. Cassini
653 ISS observation of Saturn's String of Pearls. Icarus 229, 170–180.

654 Scott, R. K., 2011. Polar accumulation of cyclonic vorticity. Geophysical and Astrophysical
655 Fluid Dynamics 105, 409–420.

Seidelmann, P. K., Archinal, B. A., A'Hearn, M. F., Conrad, A., Consolmagno, G. J., Hestroffer, D., Hilton, J. L., Krasinsky, G. A., Neumann, G., Oberst, J., Stooke, P., Tedesco, E. F., Tholen, D. J., Thomas, P. C., Williams, I. P., 2007. Report of the IAU/IAG Working Group on cartographic coordinates and rotational elements: 2006. Celestial Mechanics and Dynamical Astronomy 98, 155–180.

Tomasko, M. G., West, R. A., Orton, G. S., Teifel, V. G., 1984. Clouds and aerosols in Saturn's atmosphere. In: Gehrels, T., Matthews, M.S. (Eds.), Saturn. Univ. of Arizona Press, Tucson, pp. 150–194.

Vasavada, A. R., Hörst, S. M., Kennedy, M. R., Ingersoll, A. P., Porco, C. C., Del Genio, A. D., West, R. A., 2006. Cassini imaging of Saturn: Southern hemisphere winds and vortices. Journal of Geophysical Research (Planets) 111, E05004.

West, R. A., Baines, K. H., Karkoschka, E., Sánchez-Lavega, A., 2009. Clouds and Aerosols in Saturn's Atmosphere. In: Dougherty, M. K., Esposito, L. W., Krimigis, S. M. (Eds.), Saturn from Cassini-Huygens. p. 161.

West, R. A., Knowles, B., Birath, E., Charnoz, S., di Nino, D., Hedman, M., Helfenstein, P., McEwen, A., Perry, J., Porco, C., Salmon, J., Throop, H., Wilson, D., 2010. In-flight calibration of the Cassini imaging science sub-system cameras. Planetary and Space Science 58, 1475–1488.

Wong, A.-S., Yung, Y. L., Friedson, A. J., 2003. Benzene and Haze Formation in the Polar Atmosphere of Jupiter. Geophysical Research Letters 30, 1447.

FIGURE CAPTIONS

Figure 1. WAC images of northern high-latitudes in polar orthographic projection. The filter used to make each of the map is denoted in the panel header (see main text for their central wavelengths). The horizontal and vertical axis labels denote the planetocentric latitude along the horizontal and vertical center of the figure, respectively. Panels (a)-(c) and (e)-(h) are mosaics of two images. Panels (d) and (h) are averages of 29 high-pass spatial-filtered images as described in the main text.

Figure 2. WAC composite-color maps of northern high-latitudes in polar orthographic projection. In panel (a), the red, green, and blue channels are assigned to CB2 (as shown in Fig. 1a), MT2 (Fig. 1c) and MT3 (Fig. 1d) filters, respectively. In panel (b), the red, green, and blue channels are RED (Fig. 1e), GRN (Fig 1f) and BL1 (Fig. 1g), respectively.

Figure 3. NAC images of the northern extreme high-latitudes in polar orthographic projection. The filters are identified in the panel header as in Fig. 1. In each panel, the latitudes poleward of 90°N is from a single image, while the surrounding area is a mosaic of 7 images captured over 5 hours.

Figure 4. Same as in Fig. 3, except that the maps here are average of 7 maps captured over 5 hours.

Figure 5. Similar to Fig. 2, except that these are constructed from NAC images shown in Figs. 3 and 4.

Figure 6. (a) Zonal mean of eastward wind component (solid) and its standard deviation (dashed). (b) Zonal mean of northward wind component (solid) and its standard deviation (dashed). (c) the distribution of total number of wind vectors harvested by the TRACKER3 cloud tracking tool; it generated 274822 wind vectors from 13 pairs of polar-projected maps.

Figure 7. Map of eastward (panel a) and northward (b) wind components generated using a pair of polar-projected maps. Dark regions areas are where no trackable cloud was found. Panels (c) and (d) show the same data as panels (a) and (b) except that the gaps filled using bi-linear interpolation method.

Figure 8. (a) Relative vorticity of the flow shown in Fig. 7. (b) Divergence of the flow

shown in Fig. 7. They share the same color scale as shown at the bottom.

Figure 9. (a) Zonal mean of the relative vorticity of wind measurements in all 13 map pairs. (b) Same as panel (a), except that it shows the divergence.

Figure 10. Same as Fig. 1, except that south polar data captured in 2007 is shown here.

Figure 11. Same as Fig. 2, except that south polar data captured in 2007 is shown here.

Figure 12. NAC images of the southern extreme high-latitudes poleward of $-89.28°$S in polar orthographic projection, captured in 2008 using the CB2 filter. Panel (a)-(c) show the region in three successive images separated by approximately 45 minutes between (a) and (b), and 67 minutes between (b) and (c). Panel (d) overlays the images presented in panels (a)-(c) in red, yellow and green color channels to illustrate the cloud motion in the System III reference frame. Panels (e)-(h) show the same, except that they are rotated counterclockwise (i.e., westward) with respect to panel (a) at $0.48°$ per minute (1.4×10^{-4} radian s^{-1}) to 'freeze' the cloud motion. The features labeled A-H are discussed in the main text.

Figures and Tables for Sayanagi et al.
Cassini ISS Observation of Saturn's North Polar Vortex and Comparison to the South Polar Vortex

717

718

Camera	Year-Month-Day	Distance from Saturn	Sub-spacecraft Latitude	Solar Phase Angle	Pixel Scale
NAC	2012-11-27	418,142 – 457,351 km	37.9°N – 46.3°N	93.5°– 65.9°	2 km
WAC	2012-12-10	448,523 – 533,304 km	37.0°N – 51.8°N	105.8°– 62.5°	23 – 28 km
NAC	2008-07-14	333,218 – 390,607 km	64.8°S – 56.6°S	67.1°– 57.4°	2 km
WAC	2007-01-30	1,029,965 – 1,014,265 km	35.8°S – 39.3°S	120.5°– 102.6°	60 km

Ta le 1 When a range is given, the first number corresponds to that at the beginning of the imaging sequence, and the second to the value at the end of the sequence. Distance is measured from the center of Saturn.

Feature	Zonal × Meridional Dimensions	Morphology
A	490 × 200 km	Filamentary clouds over oval with sharp outline
B	200×160 km	Fuzzy oval
C	320×200 km	Filamentary clouds over fuzzy oval
D	120×120 km	Cyclonic spiral over fuzzy oval
E	80×80 km	Filamentary clouds over fuzzy oval
F	160×160 km	Oval with sharp outline
G	730×80 km	Train of filamentary clouds
H	80×80 km	Fuzzy oval

719

Ta le 2 List of features depicted in Fig. 12.

720

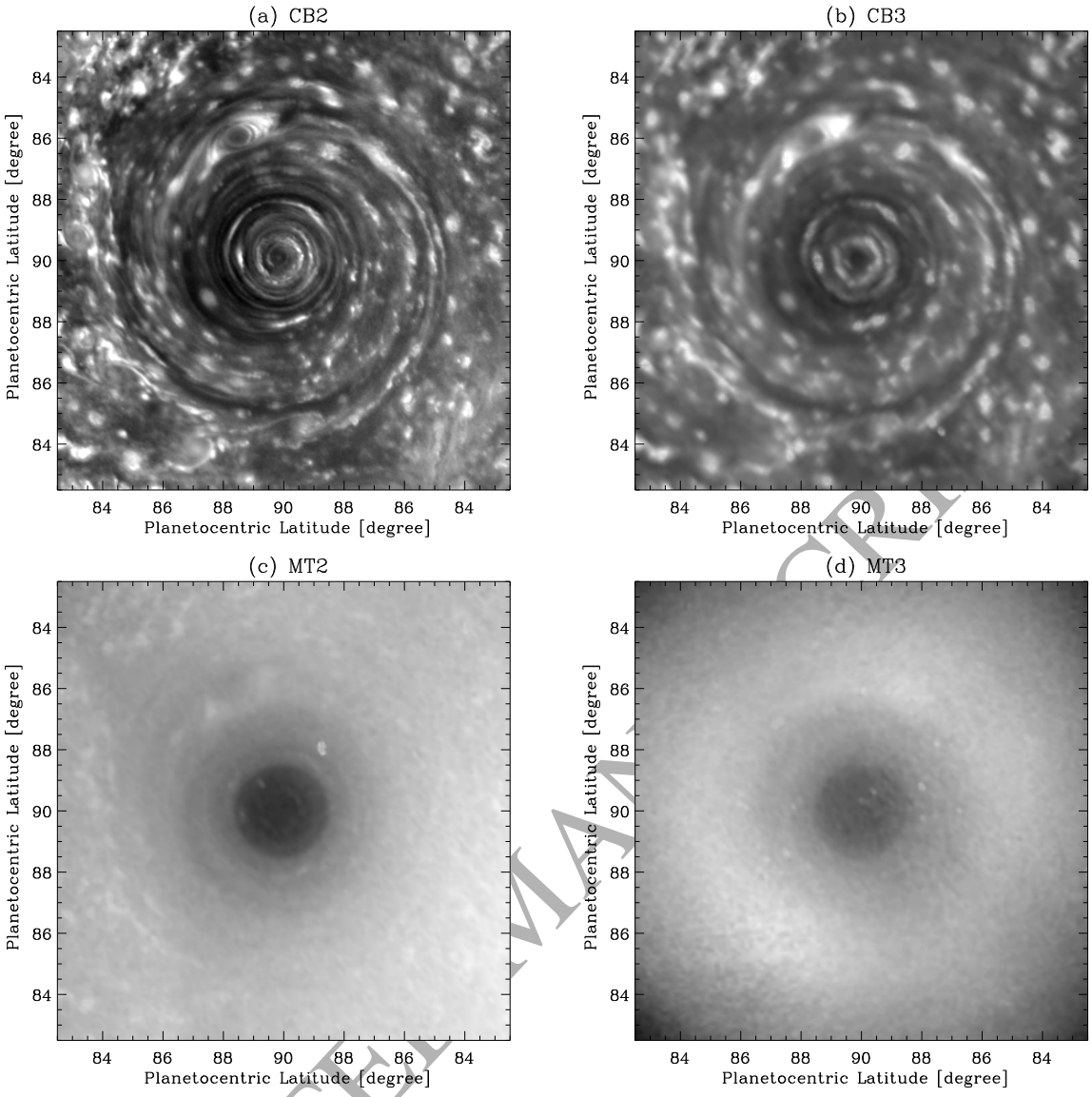

Figure 1.
WAC images of northern high-latitudes in polar orthographic projection. The filter used to make each of the map is denoted in the panel header (see main text for their central wavelengths). Panels (a)-(c) and (e)-(h) are mosaics of two images. Panels (d) and (h) are averages of 29 and 30 high-pass spatial-filtered images, respectively, as described in the main text.

721

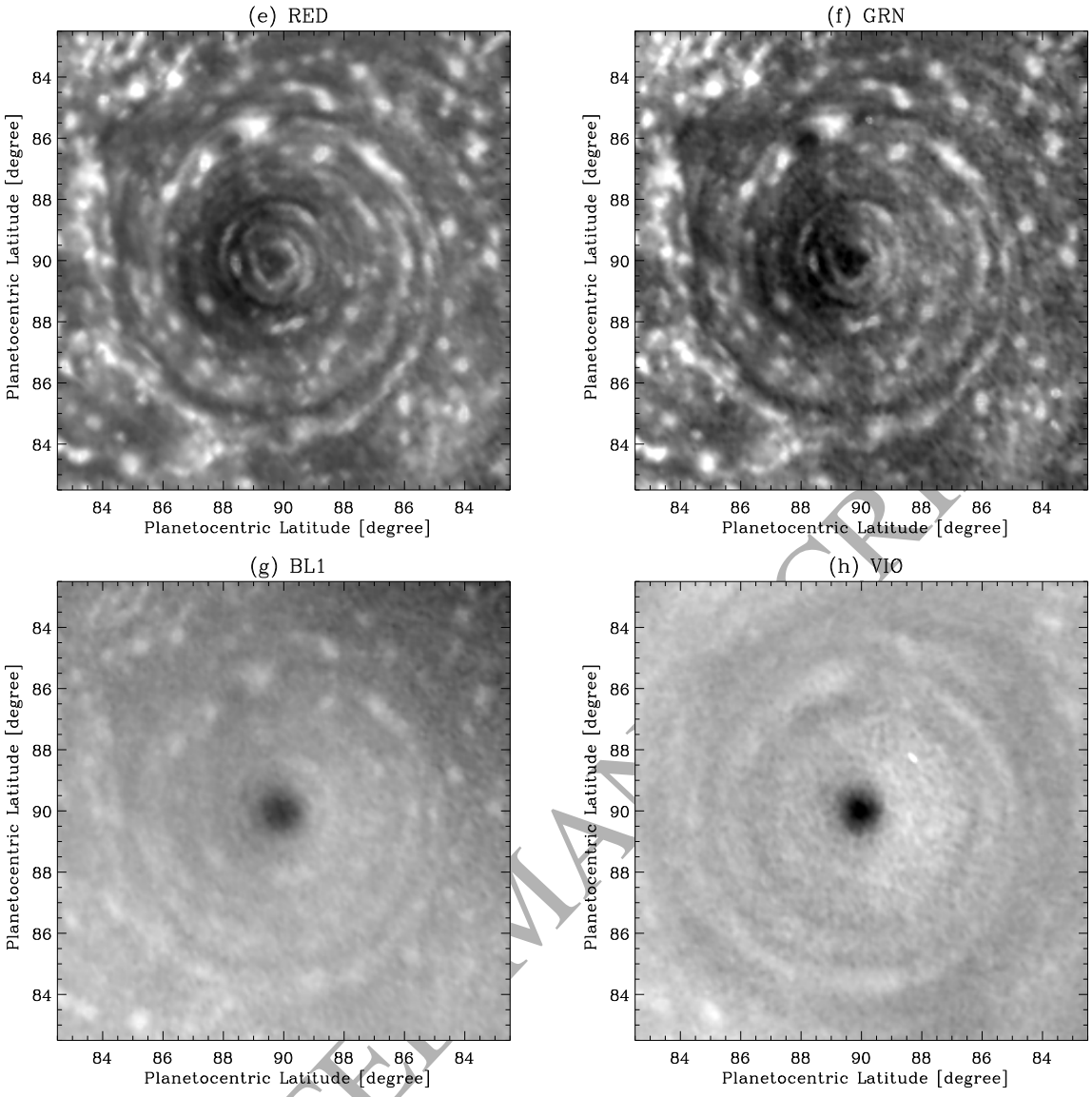

Figure 1. continued

722

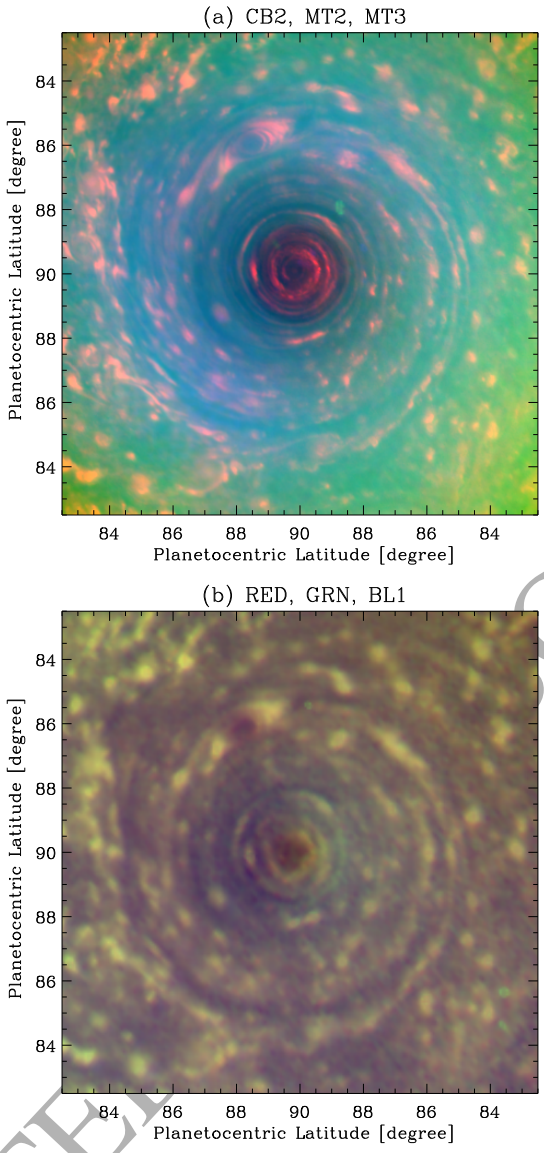

Figure 2. WAC composite-color maps of northern high-latitudes in polar orthographic projection. In panel (a), the red, green, and blue channels are assigned to CB2 (as shown in Fig. 1a), MT2 (Fig. 1c) and MT3 (Fig. 1d) filters, respectively. In panel (b), the red, green, and blue channels are RED (Fig. 1e), GRN (Fig 1f) and BL1 (Fig. 1g), respectively.

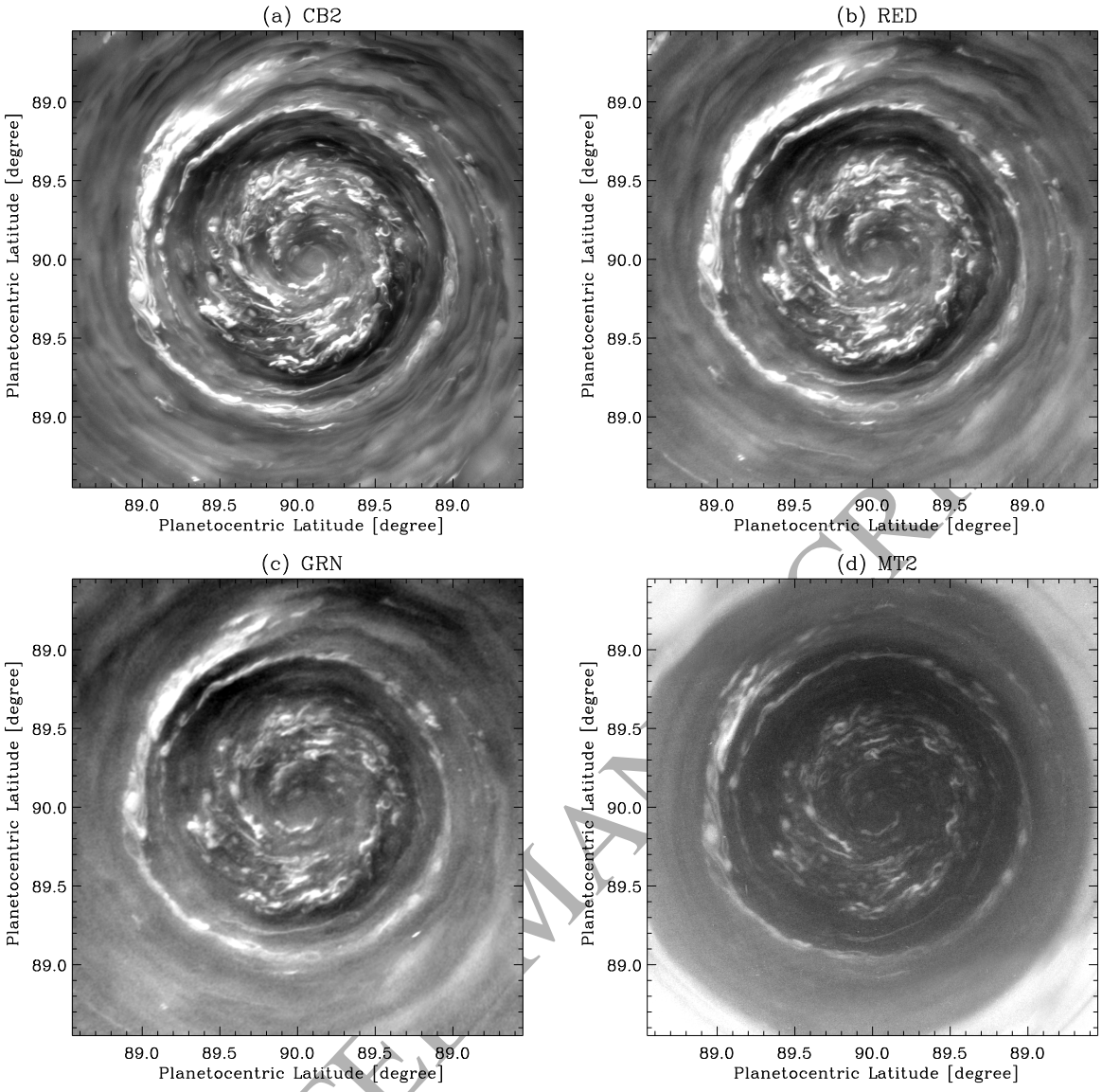

Figure 3. NAC images of the northern extreme high-latitudes in polar orthographic projection. The filters are identified in the panel header as in Fig. 1. In each panel, the latitudes poleward of 90°N is from a single image, while the surrounding area is a mosaic of 7 images captured over 5 hours.

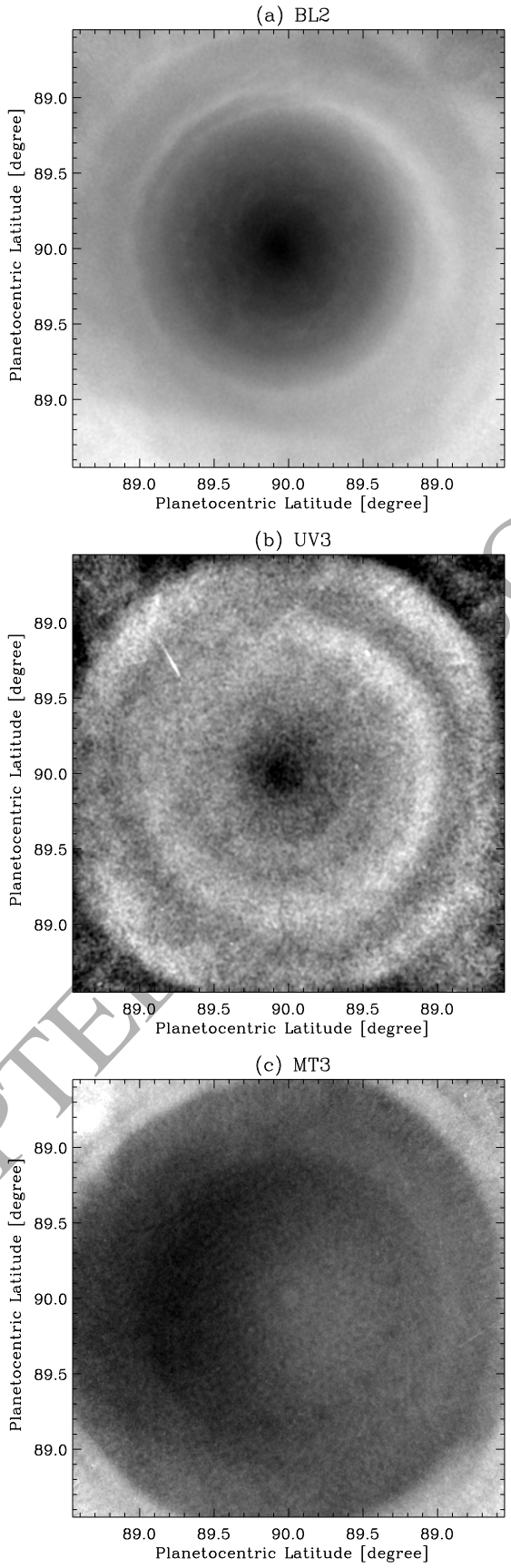

Figure 4. Same as in Fig. 3, except that the maps here are average of 7 maps captured over 5 hours.

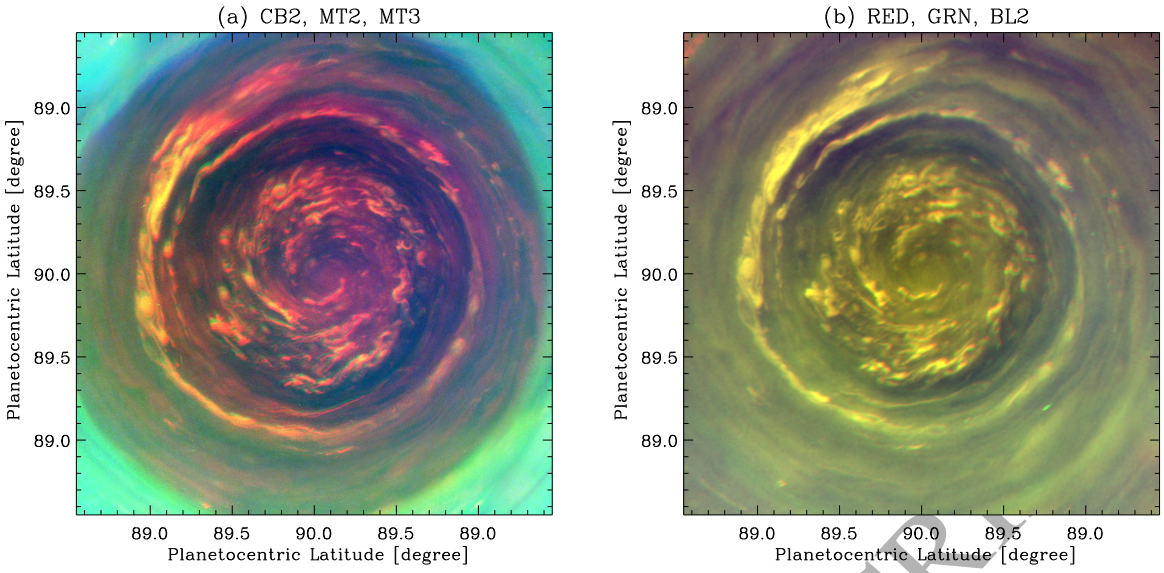

Figure 5. Similar to Fig. 2, except that these are constructed from NAC images shown in Figs. 3 and 4.

726

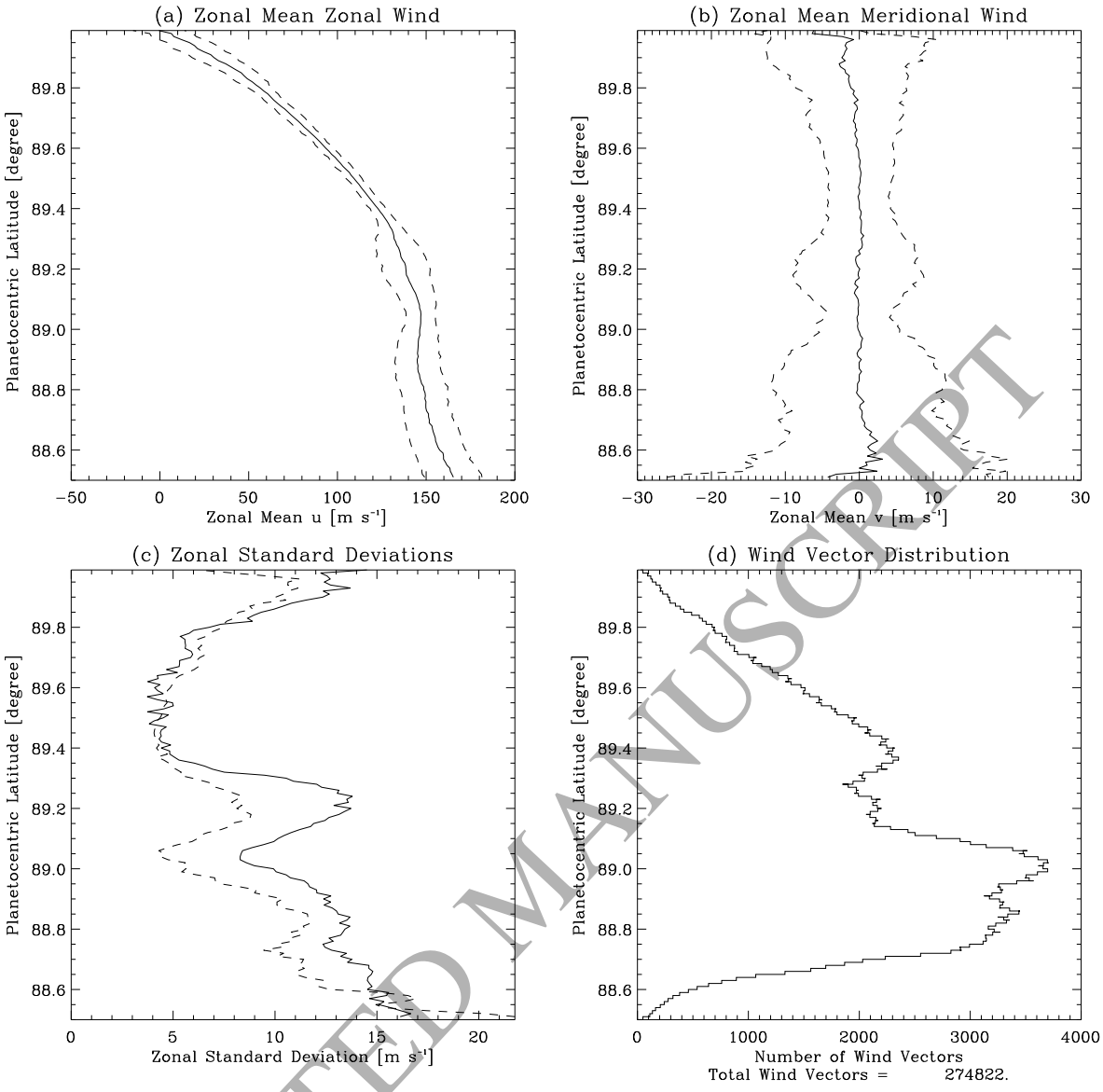

Figure 6. (a) Zonal mean of eastward wind component (solid) and its standard deviation (dashed). (b) Zonal mean of northward wind component (solid) and its standard deviation (dashed). (c) The zonal standard deviations of u (solid) and v (dashed). (d) The distribution of total number of wind vectors harvested by the TRACKER3 cloud tracking tool; it generated 274822 wind vectors from 13 pairs of polar-projected maps.

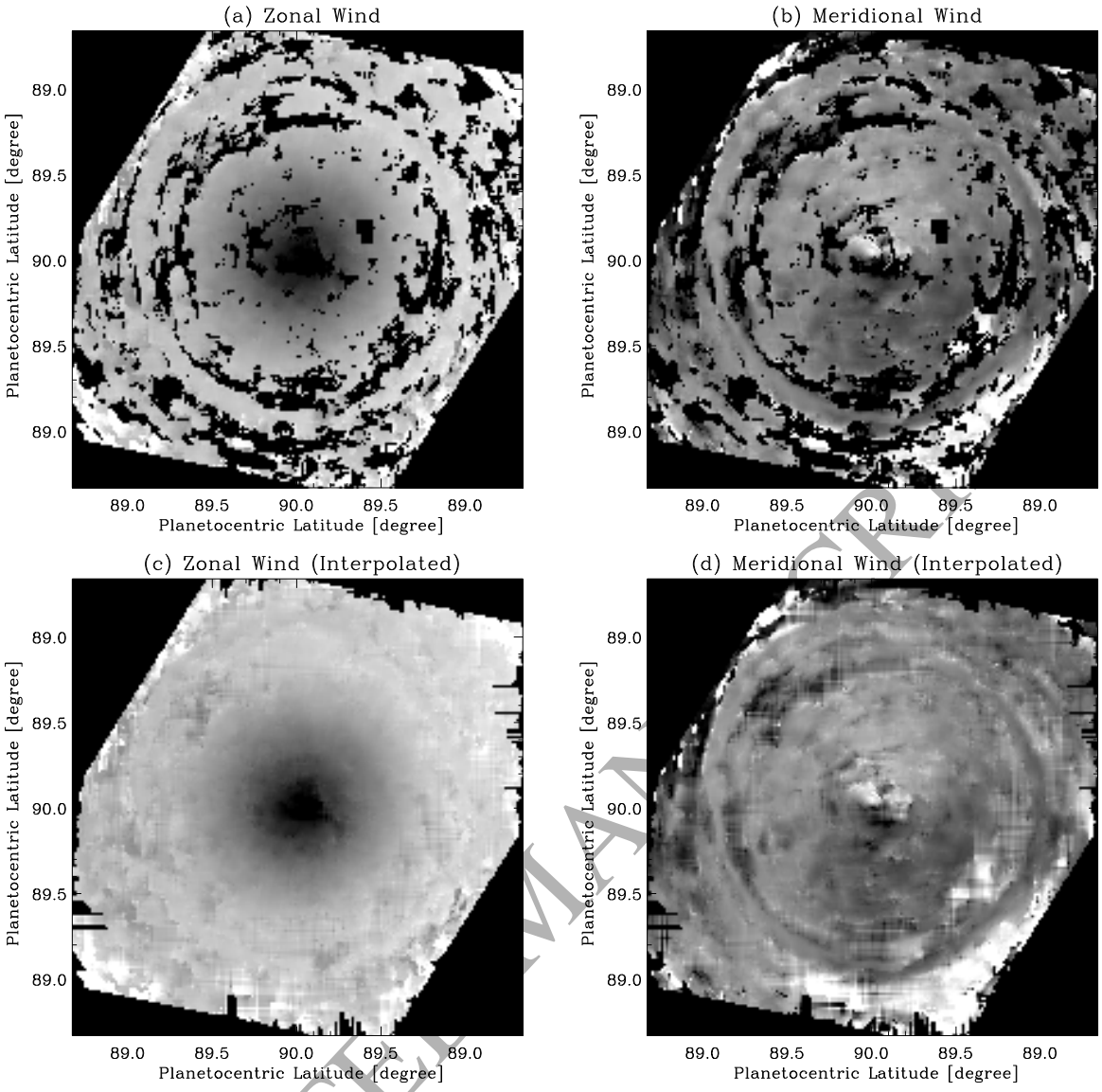

Figure 7. Map of eastward (panel a) and northward (b) wind components generated using a pair of polar-projected maps. Dark regions areas are where no trackable cloud was found. Panels (c) and (d) show the same data as panels (a) and (b) except that the gaps filled using bi-linear interpolation method.

728

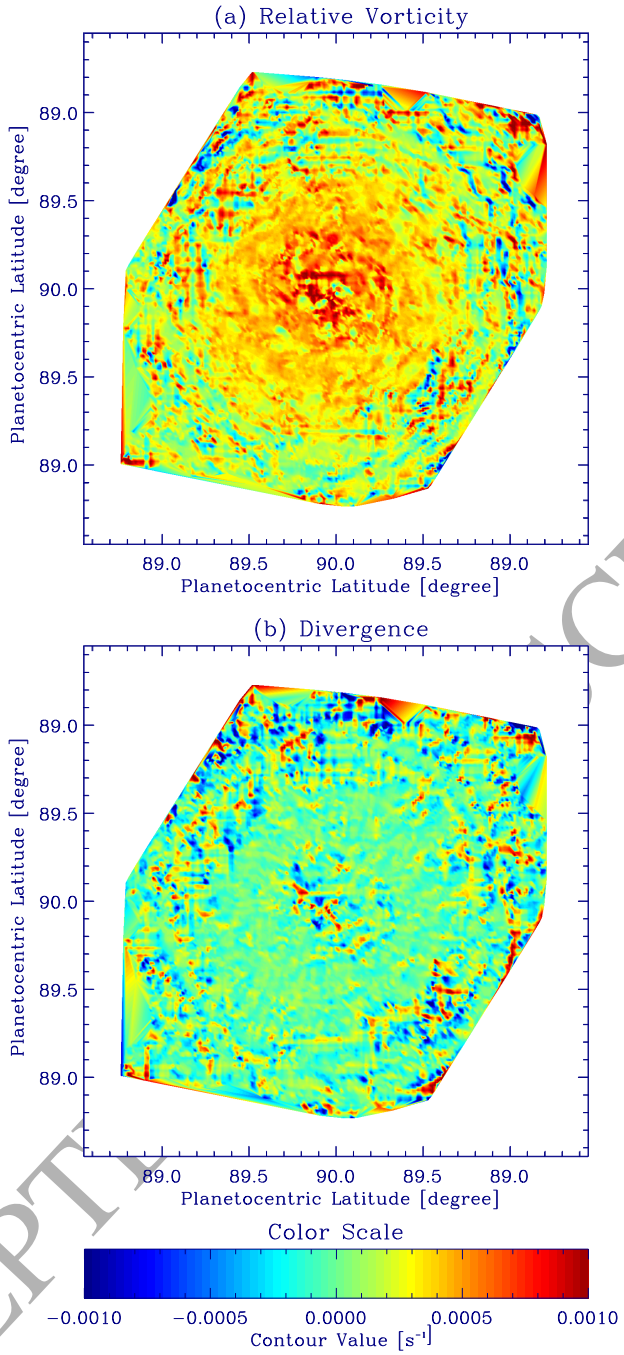

Figure 8. (a) Relative vorticity of the flow shown in Fig. 7. (b) Divergence of the flow shown in Fig. 7. They share the same color scale as shown at the bottom.

729

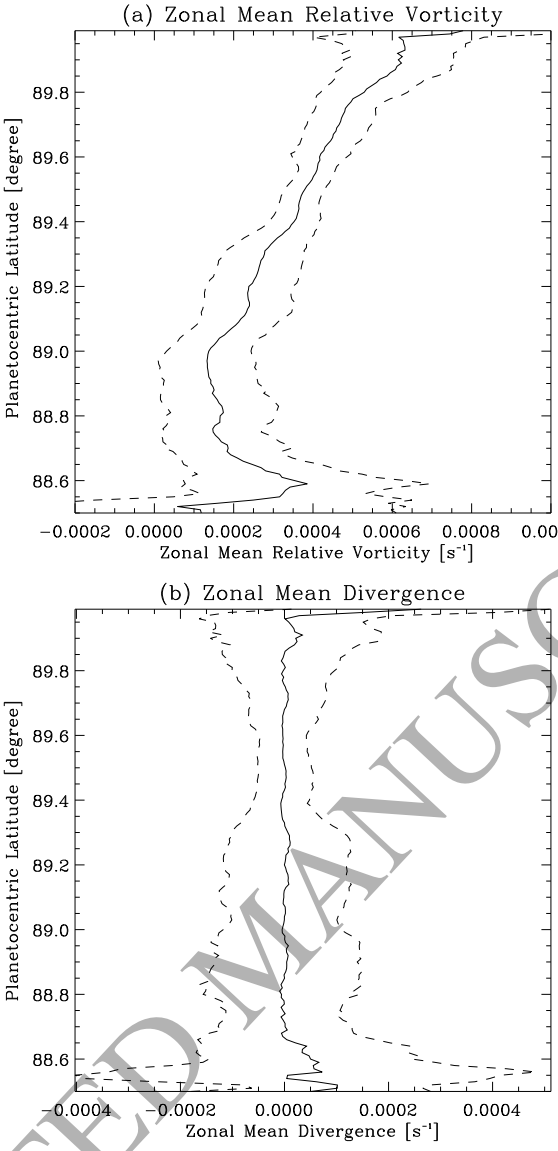

Figure 9. (a) Zonal mean of the relative vorticity of wind measurements in all 13 map pairs. (b) Same as panel (a), except that it shows the divergence.

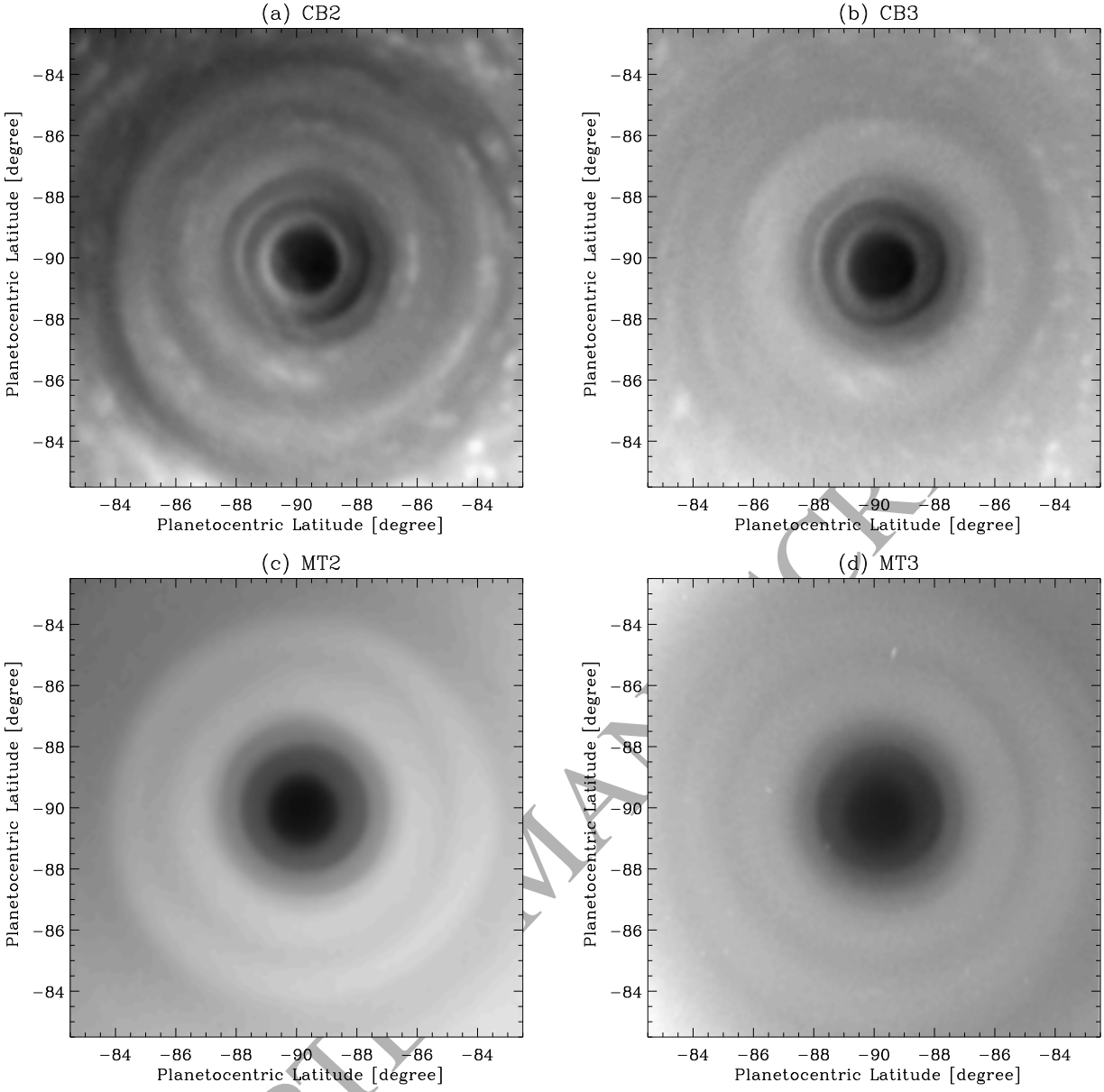

Figure 10. Same as Fig. 1, except that south polar data captured in 2007 is shown here.

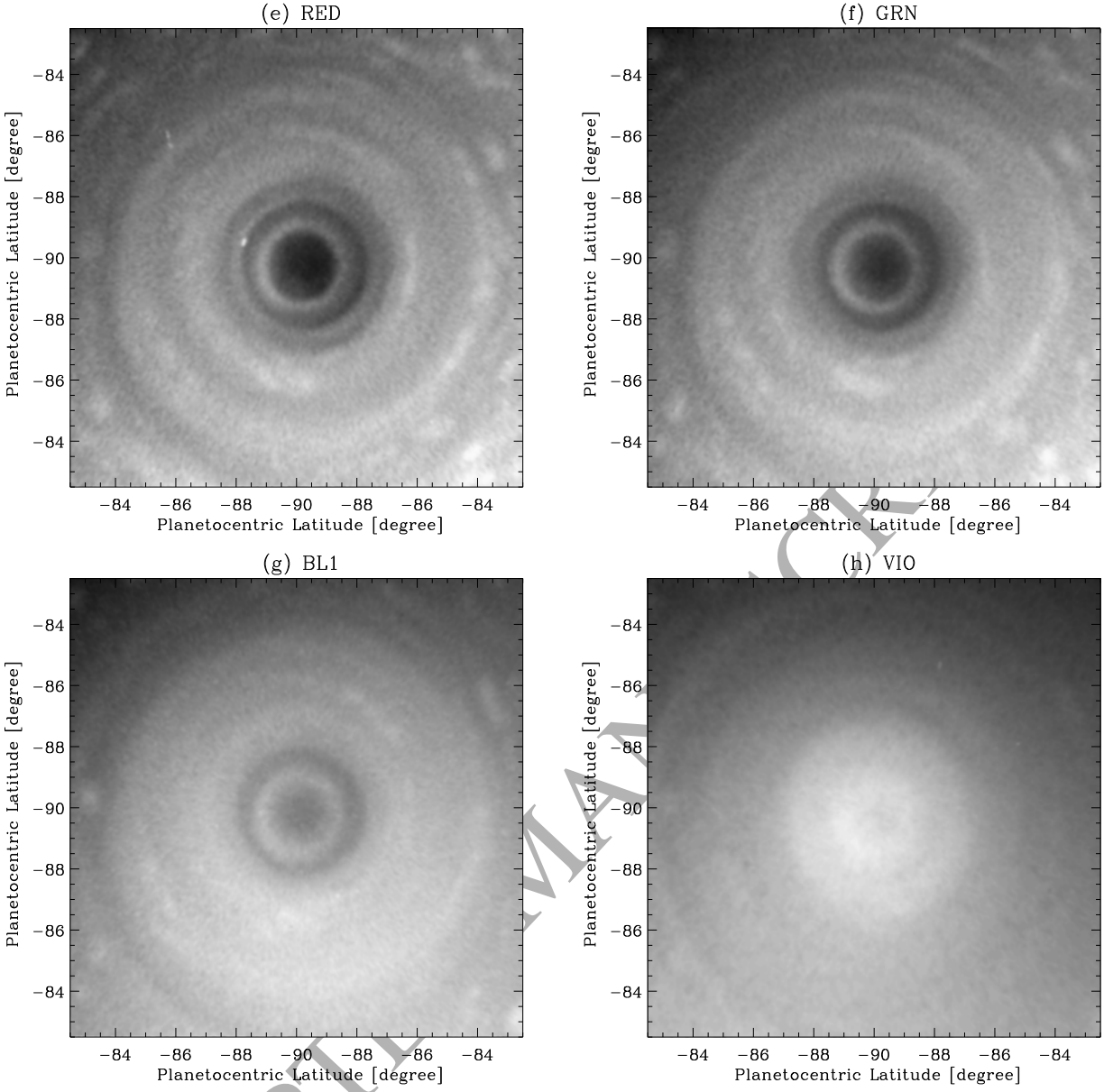

Figure 10 continued .

732

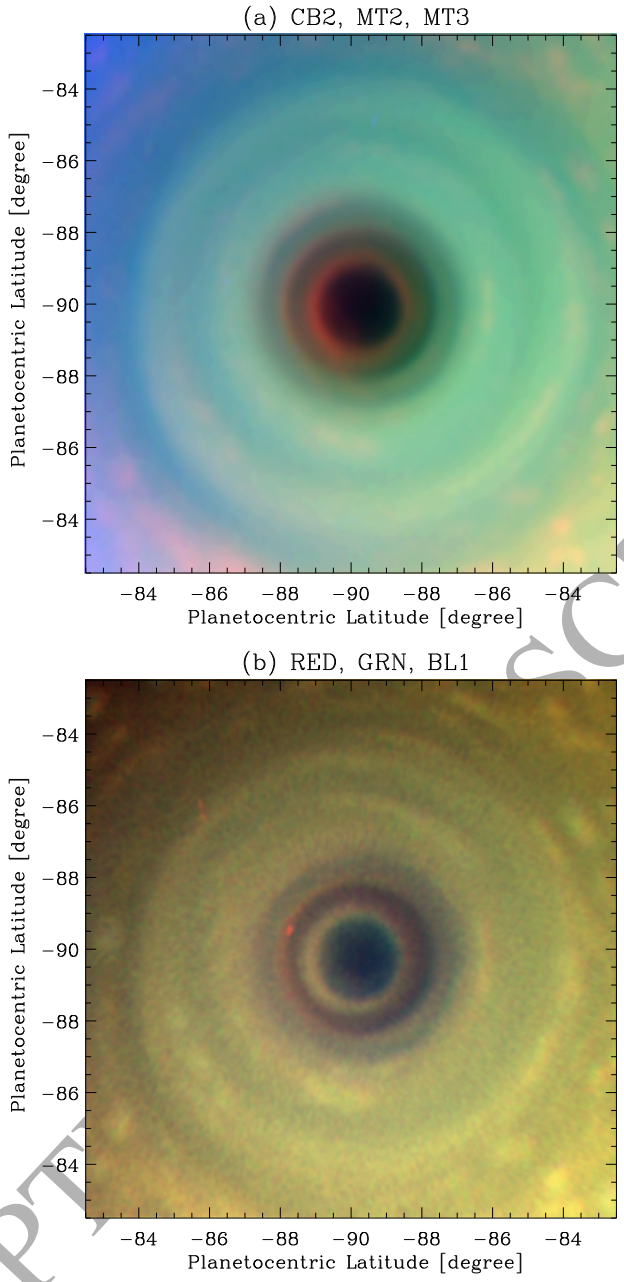

Figure 11. Same as Fig. 2, except that south polar data captured in 2007 is shown here.

733

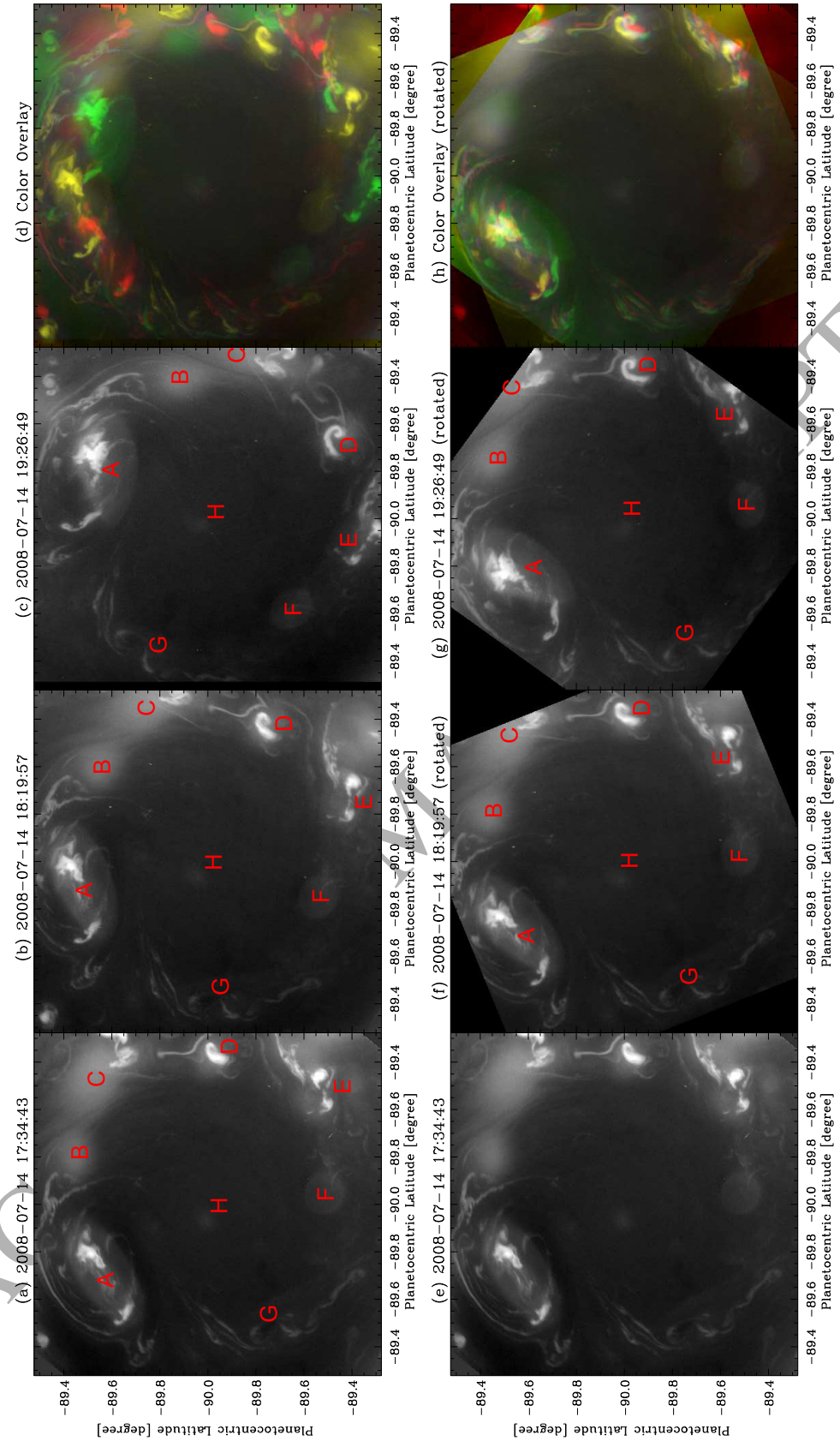

Figure 12. NAC images of the southern extreme high-latitudes poleward of −89.28°S in polar orthographic projection, captured in 2008 using the CB2 filter. Panel (a)-(c) show the region in three successive images separated by approximately 45 minutes between (a) and (b), and 67 minutes between (b) and (c). Panel (d) overlays the images presented in panels (a)-(c) in red, yellow and green color channels to illustrate the cloud motion in the System III reference frame. Panels (e)-(h) show the same, except that they are rotated counterclockwise (i.e., westward) with respect to panel (a) at 0.48° per minute (1.4×10^{-4} radian s^{-1}) to 'freeze' the cloud motion. The features labeled A-H are discussed in the main text.